CHEMISTRY

10.1126/sciadv.1501014

An iron-iron hydrogenase mimic with appended electron reservoir for efficient proton reduction in aqueous media

René Becker,[1] Saeed Amirjalayer,[1,2] Ping Li,[1] Sander Woutersen,[1] Joost N. H. Reek[1]*

The transition from a fossil-based economy to a hydrogen-based economy requires cheap and abundant, yet stable and efficient, hydrogen production catalysts. Nature shows the potential of iron-based catalysts such as the iron-iron hydrogenase (H_2ase) enzyme, which catalyzes hydrogen evolution at rates similar to platinum with low overpotential. However, existing synthetic H_2ase mimics generally suffer from low efficiency and oxygen sensitivity and generally operate in organic solvents. We report on a synthetic H_2ase mimic that contains a redox-active phosphole ligand as an electron reservoir, a feature that is also crucial for the working of the natural enzyme. Using a combination of (spectro)electrochemistry and time-resolved infrared spectroscopy, we elucidate the unique redox behavior of the catalyst. We find that the electron reservoir actively partakes in the reduction of protons and that its electron-rich redox states are stabilized through ligand protonation. In dilute sulfuric acid, the catalyst has a turnover frequency of 7.0×10^4 s^{-1} at an overpotential of 0.66 V. This catalyst is tolerant to the presence of oxygen, thereby paving the way for a new generation of synthetic H_2ase mimics that combine the benefits of the enzyme with synthetic versatility and improved stability.

INTRODUCTION

A hydrogen-based economy is a viable alternative to our current fossil-fuel–based economy (*1*), but only if hydrogen is generated in a sustainable fashion. This requires technology to reversibly store sustainable (solar or wind) energy as molecular hydrogen using water as feedstock. Although these processes are technically feasible, the required catalysts for hydrogenation and oxygen evolution are currently based on platinum and iridium, respectively (*2*). As such, the unaffordability and unavailability of materials hamper the large-scale application of these technologies. The iron-iron hydrogenase (H_2ase) enzyme catalyzes the reversible reduction of protons at rates comparable to platinum catalysts at a similar electrochemical potential (*3*). Although the applicability of the enzyme to commercial devices for proton reduction or hydrogen oxidation is complicated by elaborate growth and isolation steps and its inherent intolerance to air (*4*), its high efficiency shows that iron-based complexes can, in principle, perform this crucial reaction with a performance similar to platinum. Inspired by this, numerous synthetic complexes have been prepared as structural and functional mimics for the H_2ase active site (*5*, *6*). Most of these H_2ase mimics display proton reduction activity in organic solvents, but they often display low efficiency and stability and require a relatively high overpotential (*7*, *8*). H_2ase mimics that work efficiently in an aqueous environment while being tolerant to air have not yet been reported (*9*, *10*). Clearly, certain elements around the active site in the natural H_2ase are of crucial importance to its function. The incorporation of synthetic complexes into a natural apoenzyme results in H_2ase enzyme hybrids that can still be fully active, further demonstrating the importance of the local environment of the active site (*11*, *12*). One of the elements that received attention and was successfully installed in various mimics is the internal basic amine that functions as a proton relay. A similar proton relay was present in the nickel-based catalysts studied by Helm *et al.* (*13*), Bullock *et al.* (*14*), and Hou *et al.* (*15*), which resulted in the most efficient molecular catalysts for proton reduction known to date. The natural enzyme also preorganizes electrons using a [4Fe-4S] ferredoxin electron reservoir in close proximity to the active site. Adamska-Venkatesh *et al.* (*16*) recently demonstrated the active role of the electron reservoir in the catalytic cycle, via the so-called superreduced state of the H-cluster (H_{sred}). Long before that, Tard *et al.* (*17*) published the first structural mimic with a ferredoxin-type electron reservoir. Camara and Rauchfuss (*18*) and Lansing *et al.* (*19*) then reported on a H_2ase mimic containing a redox-active ferrocenyl phosphine that could be used for hydrogen oxidation and proton reduction catalysis. Here, we report on a synthetic H_2ase mimic that contains a redox-active phosphole ligand as an electron reservoir, which actively partakes in the reduction of protons, leading to a highly efficient and oxygen-tolerant proton reduction catalyst that operates in acidic water.

[1]Van't Hoff Institute for Molecular Sciences, University of Amsterdam, Science Park 904, Amsterdam 1098 XH, Netherlands. [2]Center for Nanotechnology (CeNTech) and Physikalisches Institut, Westfälische Wilhelms–Universität Münster, Münster 48149, Germany.
*Corresponding author. E-mail: j.n.h.reek@uva.nl

RESULTS AND DISCUSSION

In view of the essential role of the electron reservoir in the proton reduction catalytic cycle in hydrogenases, we set out to synthesize functional mimics with redox-active organic ligands. We chose a redox-active phosphole ligand, a type of ligand that has been used successfully in organic light-emitting diode applications (*20*, *21*). Various phosphole analogs can be prepared easily, including those with pyridyl moieties for improved water solubility and for supramolecular attachment of chromophores (*22*). The final hydrogenase mimic consists of an [2Fe-2S] cluster with a benzenedithiolato (μ-bdt) bridge, with the proximal iron atom bonded to the phosphorus of the phosphole ligand. The pyridyl moieties make this complex soluble in acidic water (vide infra). Furthermore, the pyridyl functions can be used for coordination to photosensitizers such as ZnTPP.

Synthesis and characterization

The pyridyl-functionalized complex **1** and its phenyl-functionalized counterpart $\mathbf{1}^{Ph}$ were prepared from the precursor complex $Fe_2(\mu\text{-bdt})(CO)_6$

by displacement of one carbonyl ligand by the corresponding phosphole ligand, either through reaction in tetrahydrofuran at reflux or by treatment with trimethylamine *N*-oxide in dichloromethane/acetonitrile at room temperature. Both methods gave a yield of around 45%, although the first method gave a cleaner crude reaction mixture, thereby facilitating purification. Complexes **1** and $\mathbf{1}^{Ph}$ are air-stable solids that can be prepared in gram scale from commercial starting materials in a convenient two-step synthesis. Both compounds were characterized by infrared (IR) (fig. S1), nuclear magnetic resonance (NMR) (^{1}H, ^{31}P) (figs. S2 to S7), and high-resolution mass spectroscopy (figs. S8 and S9). The IR spectra of both compounds show a red shift of 25 to 30 cm^{-1} compared to the parent $Fe_2(\mu\text{-bdt})(CO)_6$, as is typically observed for [2Fe-2S] carbonyl clusters (table S1).

Complex $\mathbf{1}^{Ph}$ was crystallized from pentane at −20°C, and its structure was determined by x-ray diffraction analysis (Fig. 1A). We were unable to crystallize complex **1**, but the density functional theory (DFT)–calculated structure of **1** (Fig. 1B) is in good agreement with the crystal structure of $\mathbf{1}^{Ph}$, with an average deviation in selected bond lengths between the structures of only 0.65% and an average deviation in selected angles of 0.76% (fig. S10).

Redox behavior in the absence of acid

The redox activity of the phosphole ligand in complex **1** is demonstrated by cyclic voltammetry in combination with DFT calculations and spectroelectrochemical experiments. Cyclic voltammetry in dichloromethane on a mercury electrode reveals a redox process with a cathodic peak potential of around −1.7 V (versus $Fc^{0/+}$) and anodic peak potentials of around −1.7 and −1.45 V (Fig. 2A). Controlled potential coulometry (−2.3 V) of a solution of **1** in dichloromethane on a carbon sponge electrode shows the passage of three electrons per molecule (figs. S11 and S12). The shift in the cathodic peak potential with a scan rate $\partial E_{pc}/\partial \ln(\nu)$ is 8.3 mV, which is close to the 8.5 mV [= RT/3*F*/ln(10)] expected for a three-electron process, with a rate-limiting chemical follow-up reaction after one of the electron transfers (Fig. 2A, inset) (*23*). Fitting the voltammograms (figs. S13 and S14) by simulation (figs. S15 and S16) revealed that, during the redox process, the first reduction (−1.76 V) is followed by a chemical transformation (structural rearrangement due to electron delocalization) (*24*). The second electron transfer (−1.44 V) is concerted with Fe–S bond cleavage, followed by a third reduction event (−1.64 V) (table S2).

The reduced complex $\mathbf{1}^{3-}$, generated by chemical reduction, was further studied by electron paramagnetic resonance (EPR) at room temperature. The EPR spectrum of $\mathbf{1}^{3-}$ in toluene shows a ligand-centered radical, as identified by a doublet from ^{31}P coupling (g = 2.06; A = 47 G) (Fig. 2B). The similarity of this signal to the reported radical on the free phosphole ligand (g = 2.0027; A = 28.5 G) indicates that one electron in $\mathbf{1}^{3-}$ resides at the phosphole ligand (*25*), with the other two electrons on the other part of the di-iron complex. Spectroelectrochemical experiments (Fig. 2C) reveal the IR spectrum of $\mathbf{1}^{3-}$ in which we observed an average shift in the carbonyl stretching frequency $\Delta\nu_{avg}(CO)$ of 75 cm^{-1} with respect to neutral **1**.

Because of potential inversion within the reduction process, species $\mathbf{1}^{-}$ and $\mathbf{1}^{2-}$ cannot be characterized by conventional spectroelectrochemistry or isolated after chemical reduction. However, the mono-anion $\mathbf{1}^{-}$ can be generated by photo-induced electron transfer from a supramolecularly anchored photosensitizer and identified by time-resolved IR spectroscopy (TR-IR) (*26*, *27*). The 2:1 complex of ZnTPP with **1** forms through the simple mixing of these building blocks in solution, as evidenced by ultraviolet-visible (UV-vis) titration experiments (figs. S17 to S19, table S3, and accompanying text), and the coordinated ZnTPP shows quantitative static fluorescence quenching behavior (fig. S20, table S4, and accompanying text). After the excitation of a solution of the supramolecular complex $\mathbf{1}(ZnTPP)_2$ (fig. S21) with a 630-nm laser pulse during while probing the IR spectrum with subpicosecond resolution, a new species emerged within 5 ps (Fig. 3B). Global biexponential fitting of the experimental curves at 2057, 2029, 1997, and 1970 cm^{-1} (Fig. 3C and fig. S22) shows that the excited state of the porphyrin leads to charge separation in 2.5 ps. The charge-separated state leads to recombination within 83 ps. The IR spectrum of the short-lived intermediate $\mathbf{1}^{-}$ features a $\Delta\nu_{avg}(CO)$ of 26 cm^{-1}, which is roughly one-third of the shift observed in $\mathbf{1}^{3-}$. In line with this, the DFT-calculated structure of the mono-anion $\mathbf{1}^{-}$ (Fig. 4, left) features a delocalized spin density distribution, with 0.64 e^{-} on the ligand and 0.33 e^{-} on iron. The backbone of the phosphole ligand, which is dienic in character for neutral **1**, is of intermediate dienic/aromatic character in $\mathbf{1}^{-}$, reflecting the reduction process taking place partly on the ligand. DFT calculations on species $\mathbf{1}^{2-}$ (Fig. 4, right) reveal that direduction of complex **1** leads to monoreduction of the di-iron complex and monoreduction of the ligand. The C–C bonds in the phosphole backbone are all 1.420 ± 0.004 Å, illustrating the aromatic character of the phosphole ligand in species $\mathbf{1}^{2-}$.

Comparison of the electrochemical behavior of **1** to that of the parent $(\mu\text{-bdt})Fe_2(CO)_6$ clearly shows the effect of the redox behavior of the ligand on **1**. Monoreduction of $(\mu\text{-bdt})Fe_2(CO)_6$ leads to cleavage

Fig. 1. Molecular structures of $\mathbf{1}^{Ph}$ and 1. (**A**) Crystal structure of $\mathbf{1}^{Ph}$ with displacement ellipsoids at 50% probability. (**B**) DFT-calculated (BP86, def2-TZVP) structure of **1**.

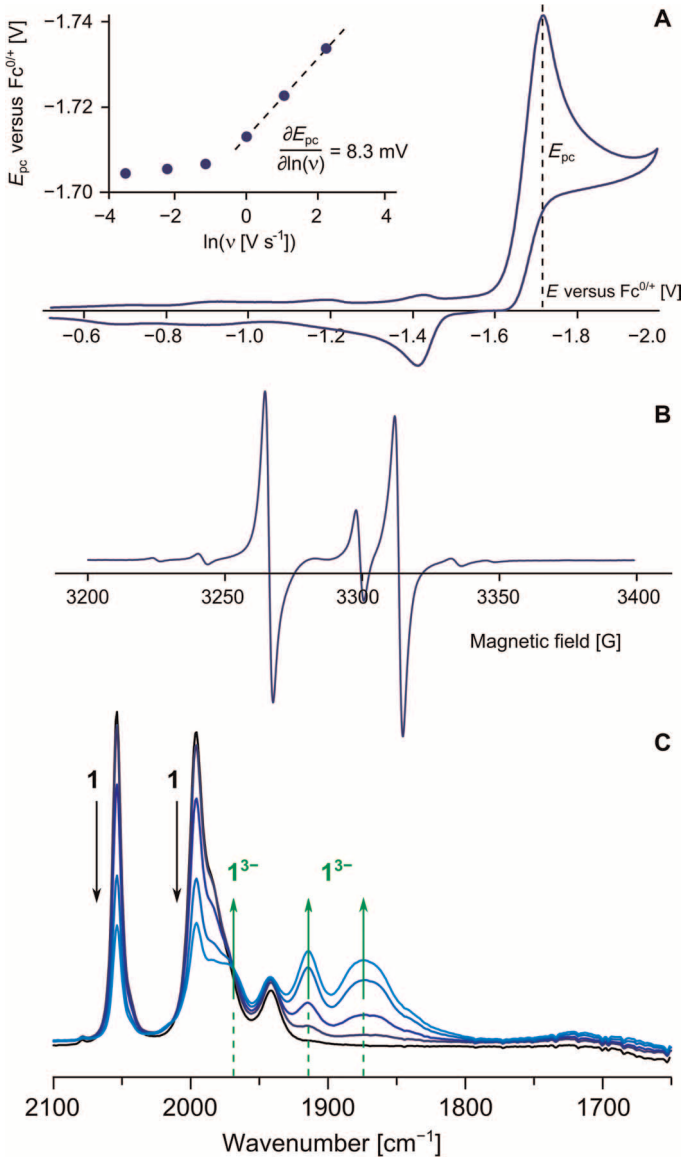

Fig. 2. Redox behavior of 1 in the absence of acid. (**A**) Cyclic voltammogram (0.1 V s^{-1}) of 1.0 mM **1** in CH_2Cl_2 containing 0.1 M nBu$_4$NPF$_6$ on a mercury working electrode. (Inset) E_{pc} variation with scan rate. (**B**) Room temperature EPR spectrum of $\mathbf{1}^{3-}$ in toluene. The singlet at 3299 G is of unknown origin. (**C**) IR spectral evolution during the reduction of 1 mM **1** in CH_2Cl_2 containing 0.1 M nBu$_4$NPF$_6$.

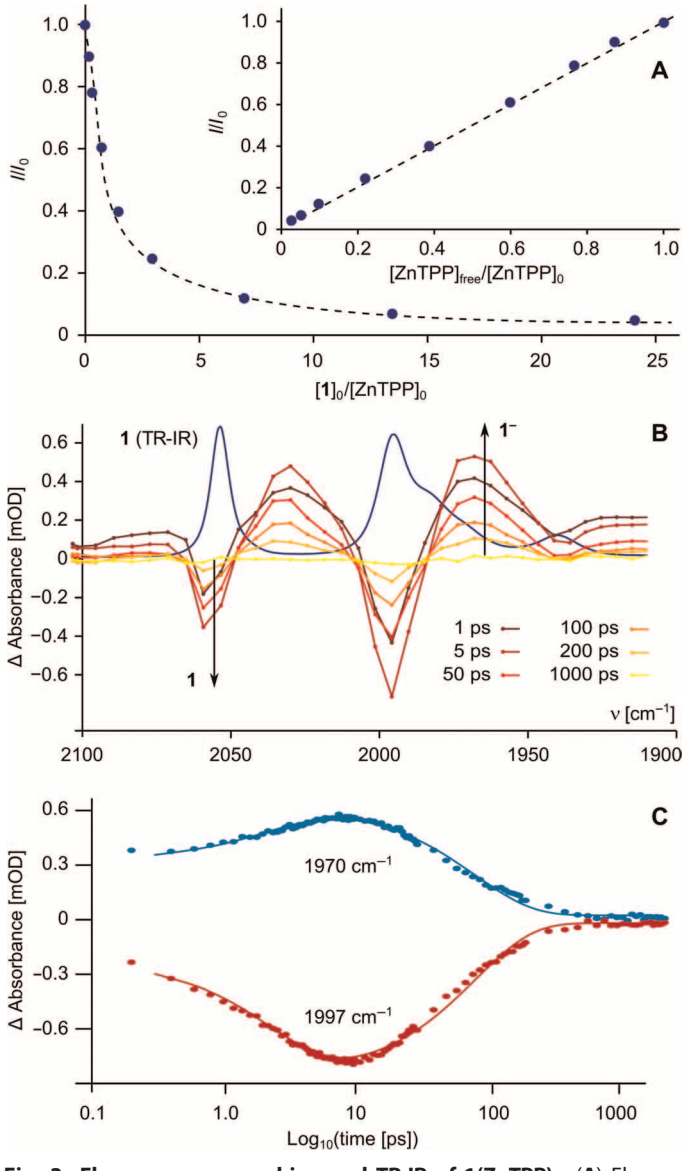

Fig. 3. Fluorescence quenching and TR-IR of 1(ZnTPP)$_2$. (**A**) Fluorescence quenching titration of a constant concentration of 80 μM ZnTPP with increasing equivalents **1** in CH_2Cl_2. Fluorescence intensity (λ_{em} = 645 nm) versus equivalents **1** and (inset) versus the ratio of free ZnTPP showing full static quenching. (**B**) Spectral evolution during TR-IR of **1**(ZnTPP)$_2$. (**C**) Rise and decay profiles plus global biexponential fitting from TR-IR at four wavelength maxima (only two are shown for clarity). mOD, milli optical density.

of the Fe–S bond (*28*), as is evident from the DFT-calculated structure. In contrast, the [2Fe-2S] butterfly structure of $\mathbf{1}^-$ remains intact, with an average Fe–S bond elongation of 0.02 Å, because the electron mainly resides on the ligand. The second reduction of the complex to give $\mathbf{1}^{2-}$ leads to a singly reduced ligand and singly reduced di-iron complex, which is comparable to the mono-reduced parent (μ-bdt)$Fe_2(CO)_6$. Indeed, this leads to Fe–S bond rupture to form a structure that is able to accept another electron. This suggests that, in species $\mathbf{1}^{3-}$, two electrons are located on the di-iron complex and one electron is located on the ligand. These results highlight the effect of the use of redox-active ligands on this type of hydrogenase mimics and show that, as a consequence, the redox properties of **1** are similar to those of the H-cluster of the H_2ase enzyme. In the natural system, one-electron reduction of the H_{ox} state is localized on the [2Fe-2S] cluster, mediated by the [4Fe-4S] electron reservoir (*29*). Two-electron reduction leads to H_{sred}, with one electron on [2Fe-2S] and one on the ferredoxin [4Fe-4S] cluster (*16*).

Electrocatalysis in dichloromethane

In the presence of acid, complex **1** is catalytically active in the reduction of protons. Cyclic voltammetry in dichloromethane containing Et_3NHBF_4 on a mercury electrode shows two well-resolved reduction

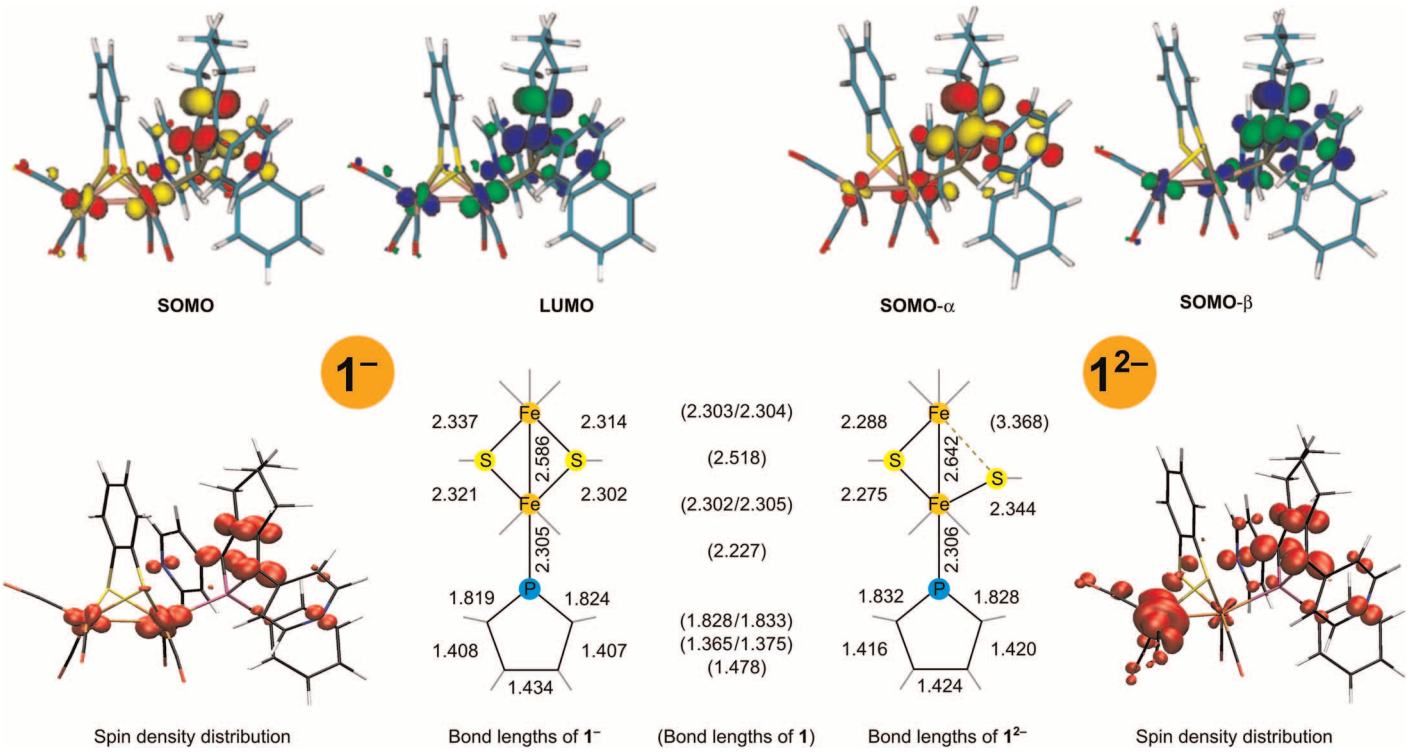

Fig. 4. DFT-calculated properties of 1^- and 1^{2-}. Illustration of the DFT-calculated (BP86, def2-TZVP) frontier orbitals (**top**) and spin density distributions (**bottom**) of 1^- and 1^{2-} (triplet). Selected bond lengths (**middle**) of **1**, 1^-, and 1^{2-} illustrate both Fe–S bond elongation followed by rupture, and aromatization of the phosphole backbone upon monoreduction and direduction. SOMO, singly occupied molecular orbital; LUMO, lowest unoccupied molecular orbital.

waves, followed by a catalytic wave that increases in amplitude with increasing acid concentration (Fig. 5). This shows that complex **1** needs to be activated by reduction before the active species can enter the catalytic cycle.

The first redox process (**1** ↔ **2**) has a cathodic peak potential of around −1.4 V (versus $Fc^{0/+}$), roughly 0.3 V more positive than in the absence of acid (Fig. 6A and figs. S23 to S26). This anodic shift indicates that at least one proton is involved in the redox process and that the first process involves a proton-coupled electron transfer (section S7.2) because Et_3NHBF_4 is not acidic enough to protonate **1** (fig. S27). To elucidate the operating mechanism of this first redox wave, we performed a peak potential analysis of a series of voltammograms measured at varying acid concentrations and scan rates (Fig. 6B and figs. S28 and S29). In the pure kinetic zone, the shift in the cathodic peak potential with scan rate $\partial E_{pc}/\partial \ln(v)$ was 12.5 mV, close to the 12.9 mV [= RT/2*F*/ln(10)] expected for a two-electron process, with a rate-limiting chemical follow-up reaction after the first electron transfer (*23*). The shift in the cathodic peak potential with acid concentration $\partial E_{pc}/\partial \ln([Et_3NHBF_4])$ was 25.2 mV, indicating that two protons are transferred after the first electron transfer. Digital simulation of the voltammograms (fig. S30) revealed an overall redox process involving two proton and two electron transfers [electrochemical, chemical, chemical, electrochemical (ECCE) process at −1.44 and −1.18 V] (table S5). The IR spectrum of the resulting species **2** was recorded using spectroelectrochemistry on a gold-amalgam working electrode (Fig. 6C) and shows CO stretching frequencies (2041, 1977, and 1915 cm^{-1}) similar to **1** [$\Delta\nu_{avg}(CO)$ = 15 cm^{-1}]. This relative small shift is indicative of the formation of a mono-reduced iron hydride, and the remaining electron density and proton are located on the phosphole ligand (*27*, *30*–*32*). No bands belonging to a bridging carbonyl ligand were observed.

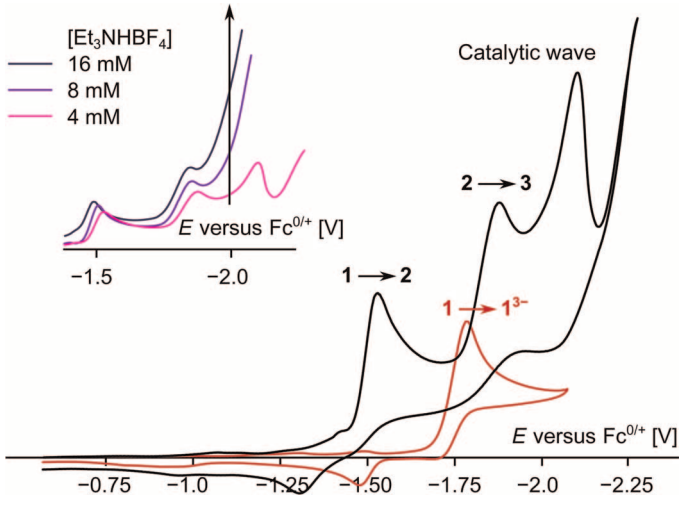

Fig. 5. Catalysis in dichloromethane. Cyclic voltammetry (0.1 V s^{-1}) of 1.0 mM **1** in CH_2Cl_2 containing 0.1 M nBu_4NPF_6 and 4.0 mM Et_3NHBF_4 on a mercury working electrode. (**Inset**) A catalytic wave that increases in amplitude with increasing acid concentration.

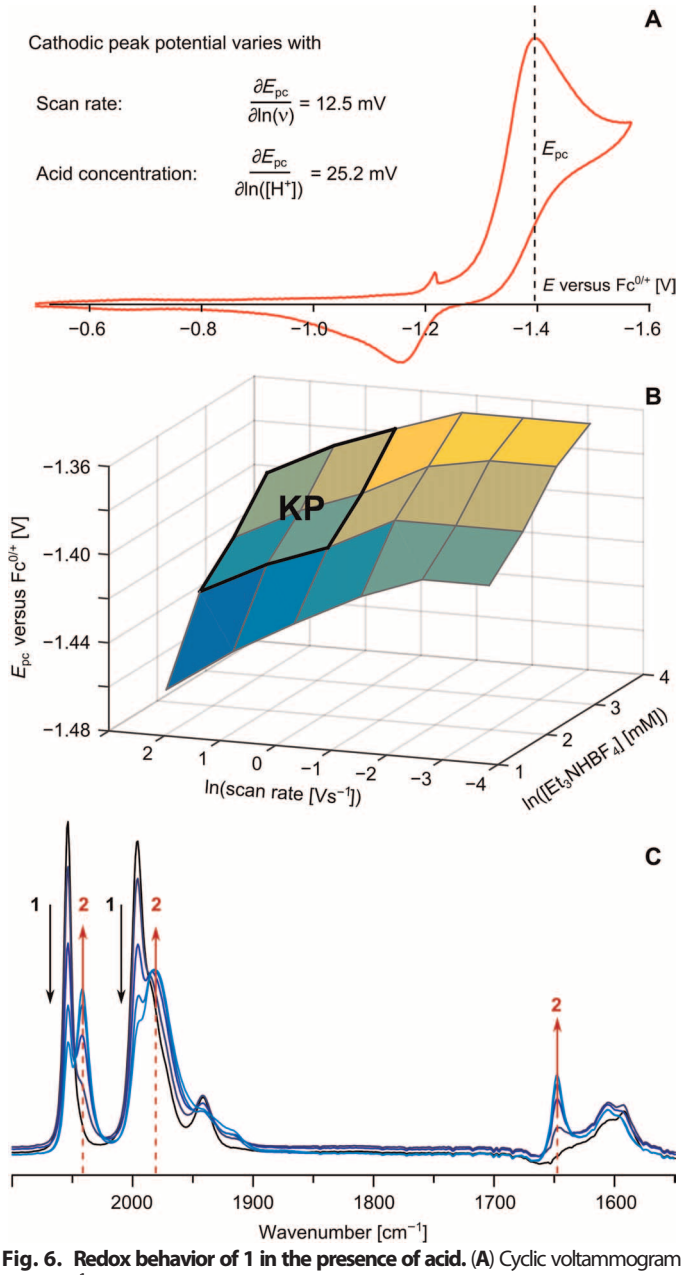

Fig. 6. Redox behavior of 1 in the presence of acid. (**A**) Cyclic voltammogram (0.1 V s^{-1}) of 1.0 mM **1** in CH_2Cl_2 containing 0.1 M nBu_4NPF_6 and 4.0 mM Et_3NHBF_4 on a mercury working electrode. (**B**) Peak potential analysis depicting the pure kinetic (KP) zone. (**C**) IR spectral evolution (first redox wave) during the reduction of 1 mM **1** in CH_2Cl_2 containing 0.1 M nBu_4NPF_6 and 4.0 mM Et_3NHBF_4 on a AuHg working electrode.

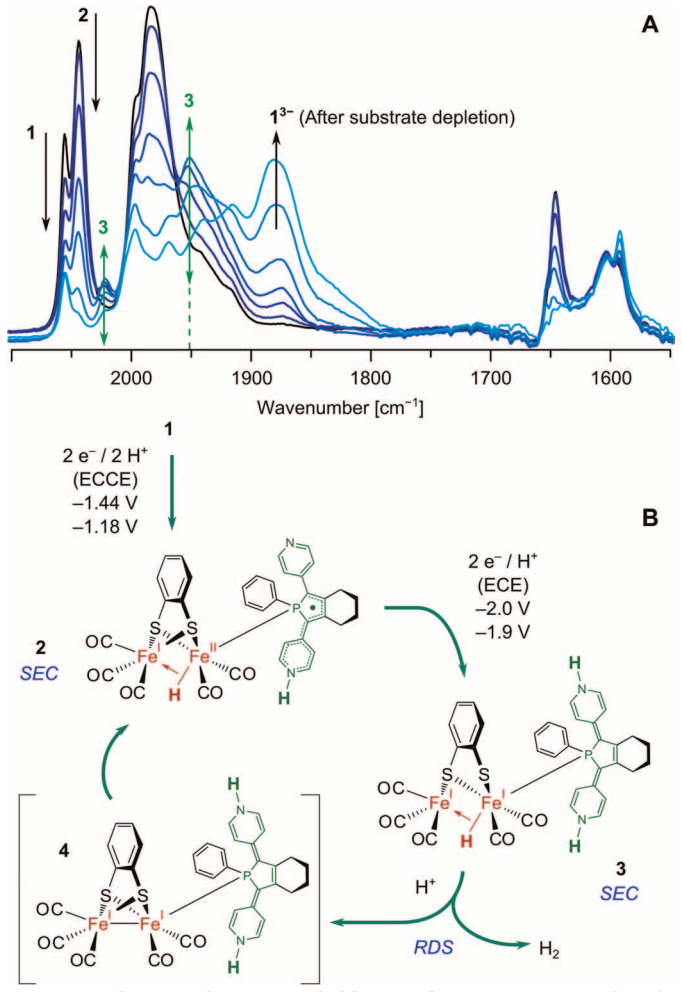

Fig. 7. Catalytic mechanism in dichloromethane. (**A**) IR spectral evolution (second redox wave and catalytic wave combined) during the reduction of 1 mM **1** in CH_2Cl_2 containing 0.1 M nBu_4NPF_6 and 4.0 mM Et_3NHBF_4 on a AuHg working electrode. (**B**) Proposed mechanism of proton reduction by (activated) **1** in dichloromethane. SEC, spectroelectrochemistry; RDS, rate-determining step.

Modeling of the cyclic voltammogram in Fig. 5 reveals the nature of the second redox process (**2** ↔ **3**) as a two-electron and single-proton process (ECE process at −2.0 and −1.9 V), leading to the catalytic resting state **3**. Spectroelectrochemical analysis of the catalytic wave (Fig. 7A) reveals the CO stretching frequencies of the resting state **3** at 2020, 1951, 1931, 1904, and 1875 cm^{-1} with a $\Delta\nu_{avg}$(CO) of 57 cm^{-1} with respect to **1**. This shift (42 cm^{-1} with respect to **2**) is much smaller than that expected for a two-electron reduction on iron, indicating that both electrons are equally distributed over iron and ligand, leading to a resting state in which two electrons (and two protons) are stored on the phosphole ligand. Comparison of the IR region between 1570 and 1670 cm^{-1} to the IR spectra of the reduced and protonated states of 4,4′-bipyridine (*33*) confirms the reduction and protonation states of the ligand (figs. S31 and S32 and table S6). Modeling of the redox and chemical processes in the catalytic wave shows that the only plausible catalytic mechanism is of the ECEC type (Fig. 7B, fig. S33, and table S7). Advancing through the catalytic cycle, the resting state **3** is protonated ($k = 10^5$ M^{-1} s^{-1}) to release H_2 in a rate-determining step. The newly formed species **4** has the same overall reduction/protonation state as **2**. Spectroelectrochemistry could not successfully identify species **4**, which is caused by the very short lifetime of this species under catalytic conditions. It seems reasonable that **4** is converted into **2** by an (overall) intramolecular proton and electron transfer from the phosphole ligand to iron.

One of the interesting features of the catalytic mechanism is that, in the catalytic cycle, an electron is transferred from the ligand to an iron center. The ligand thus acts as an electron reservoir during catalysis,

similar to the enzyme's catalytic cycle where the H_{sred} state is protonated with concomitant electron transfer from the ferredoxin cluster to [2Fe-2S] (*16*). A major implication of this peculiar behavior is the leveling of redox potentials within the catalytic cycle (a difference of only 0.1 V). In contrast, weak acid catalysis using the parent compound (μ-bdt)$Fe_2(CO)_6$ shows that this complex operates with a similar ECEC mechanism but with the reduction potentials spaced almost 0.8 V apart (−1.31 and −2.08 V) (*28*). Redox potential leveling is essential for both electron transfers to occur with similar driving force (*10*). In catalyst **1**, this leveling is induced by a balancing of charges through protonation of the ligand concomitant with electron transfer, which is clearly seen in the anodic shift in the reduction potential by ca. 0.3 V upon addition of a proton source. In control experiments carried out with the analogous complex $\mathbf{1}^{Ph}$ with phenyl groups instead of pyridyl moieties, such shift was not seen, and the resulting redox reaction follows an ECE mechanism instead of the ECCE mechanism observed for **1** (figs. S34 to S36). This signifies the role of the pyridyl moiety in the reduction process and illustrates the applicability of the dipyridylphosphole as a redox and proton-reactive ligand.

Catalysis in aqueous media

Complex **1** at 2.0 μM concentration is soluble in 1 M sulfuric acid as a result of the protonation of the pyridyl moieties attached to the ligand building block, enabling proton reduction catalysis in water. Cyclic voltammetry using a gold-amalgam working electrode shows catalytic current densities up to 50 mA cm^{-2} with a half-wave potential of −0.7 V normal hydrogen electrode [versus normal hydrogen electrode (NHE)] and hydrogen evolution clearly visible on the electrode (Fig. 8A). Oxygen sensitivity is generally one of the critical properties of hydrogenase enzymes and many of the synthetic mimics, complicating their application in devices. We were pleased to find that catalysis in air-saturated solution retained 60% of catalytic performance (in terms of current densities) compared to experiments performed in properly degassed solvent (Fig. 8B), indicating that these mimics are not only water-soluble but also air-tolerant, both highly desired properties for H_2ase mimics (*7*, *8*).

In 1 M H_2SO_4, plateau currents (required to establish catalytic rate constants) were not obtained, most likely as a result of rapid depletion of the acid. To determine a rate constant for the catalytic process in 1 M H_2SO_4, we performed foot-of-the-wave analysis to obtain a hypothetical value of 50 mA cm^{-2} for the plateau current density j_{pl} (fig. S37) (*34*). For foot-of-the-wave analysis, the dominant redox couple E_{cat} for the catalyst under catalytic conditions must be known. Plateau currents were obtained in 1 M Na_2SO_4 (acidified with concentrated sulfuric acid to the desired pH) (Fig. 9A). Under these conditions, the catalytic half-wave potential converged to −0.66 V (versus NHE) for pH < 1.5 (Fig. 9B), and this potential was used as the dominant redox couple E_{cat} for the catalyst in 1 M H_2SO_4. Moreover, whether the catalyst is in a homogeneous solution or adsorbed on the electrode must be determined. In acidified 1 M Na_2SO_4, the linear dependence of catalytic current on proton concentration indicates that the catalyst is adsorbed on the gold-amalgam electrode (Fig. 9C). Because redox waves belonging to **1** are masked by catalytic current, we synthesized a water-soluble mimic of protonated **1** by alkylation at the pyridyl nitrogen atoms. This mimic was prepared by reacting **1** with 2 eq of $(Et)_3O{\cdot}BF_4$ in dichloromethane at room temperature and characterized by NMR (^1H, ^{31}P) and IR spectroscopy (figs. S38 to S40). Cyclic voltammetry

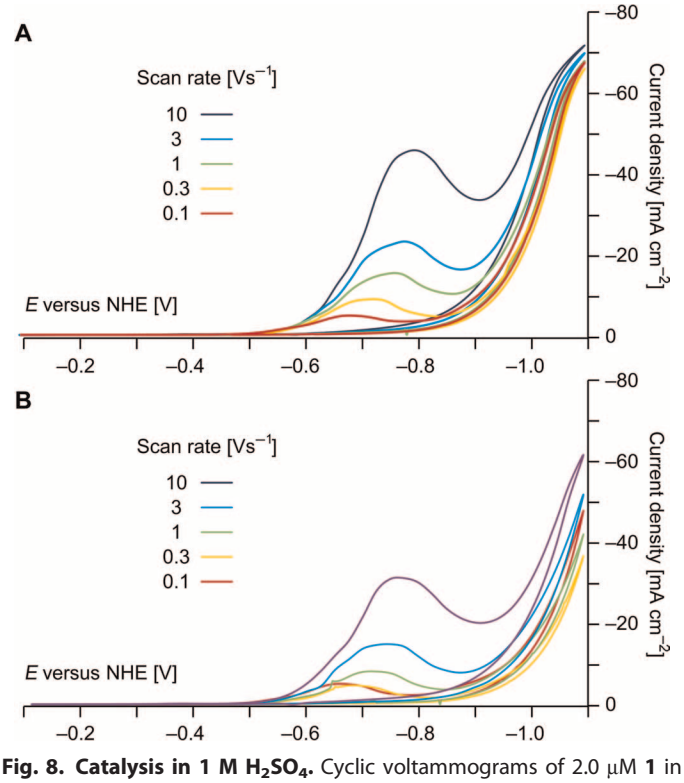

Fig. 8. Catalysis in 1 M H_2SO_4. Cyclic voltammograms of 2.0 μM **1** in 1 M H_2SO_4 on a AuHg working electrode at different scan rates. (**A**) Under a nitrogen atmosphere. (**B**) Under air.

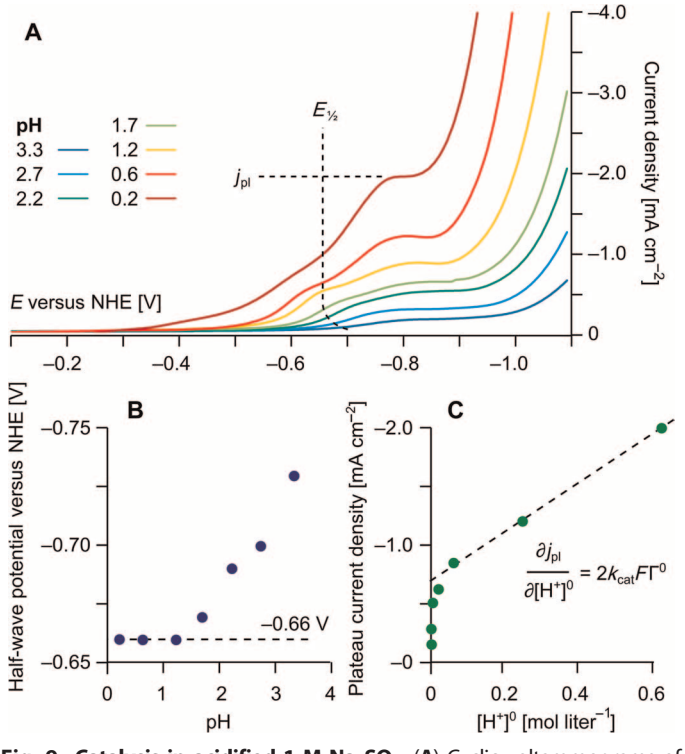

Fig. 9. Catalysis in acidified 1 M Na_2SO_4. (**A**) Cyclic voltammograms of 2.0 μM **1** in 1 M Na_2SO_4 (pH adjusted with concentrated H_2SO_4) on a AuHg working electrode at 0.1 V s^{-1} at different pH values. (**B**) Half-wave potential versus pH. (**C**) Plateau current density versus proton concentration.

of this pyridine-ethylated analog $Et_2\mathbf{1}\cdot(BF_4)_2$ in neutral water shows an adsorption wave leading to a surface concentration Γ^0 of 0.73×10^{-11} mol cm^{-2} (figs. S41 and S42) (*35*). Assuming a similar behavior for **1** in acidic water, this surface concentration was used to determine catalytic efficiency. In line with catalysis from surface-adsorbed catalyst molecules, the addition of acetonitrile to the solution led to a decrease in catalytic current (noticeable from approximately 1% v/v) as a result of the desorption of the catalyst from the surface. In a separate control experiment, the free ligand was also used as a proton reduction catalyst but showed no activity (figs. S43 and S44).

The obtained catalytic rate constant in 1 M H_2SO_4 (calculated using $j_{pl} = 2k_{cat}F\Gamma^0[H^+]^0$) (*36*, *37*) is 3.5×10^4 M^{-1} s^{-1}, close to that found in dichloromethane (10^5 M^{-1} s^{-1}), suggesting that the catalytic mechanism does not change significantly by changing the solvent. Moreover, turnover numbers (TONs) during one cyclic voltammetric scan are on the order of 10^3 to 10^4 (table S8), confirming the stability of the catalyst. With the rational benchmarking approach outlined by Artero and Savéant (*38*), a catalytic Tafel plot can be constructed from $TOF_{max} = 2k_{cat}[H^+]^0 = 7.0 \times 10^4$ s^{-1} and an overpotential of 0.66 V. Clearly, catalyst **1** displays high rates in aqueous phase but at an overpotential that is still higher than the natural enzyme.

CONCLUSION

We report here the first di-iron H_2ase mimic that is equipped with a redox-noninnocent phosphorus ligand. The redox-active ligand functions as an electron reservoir, donating an electron to the active site during the catalytic cycle when needed, in resemblance to the natural H_2ase system where an iron-sulfur cluster near the active site is responsible for this function. The catalyst operates in an aqueous environment, is oxygen-tolerant, and displays high TON and turnover frequency (TOF), which is a major step toward the development of catalysts for hydrogen-producing devices. Now that we have demonstrated that H_2ase mimics with electron reservoirs are easily accessible via a redox-active phosphorus ligand, further development should be directed toward analogs that operate at lower overpotentials and can be efficiently implemented in devices (for example, by anchoring to electrodes or metal-organic frameworks).

MATERIALS AND METHODS

General procedures

All syntheses were carried out under a nitrogen atmosphere using standard Schlenk techniques. All purifications involving column chromatography were performed in air with non-degassed solvents. Dichloromethane used for synthesis, UV-vis, fluorescence, electrochemistry, and spectroelectrochemistry was distilled over calcium hydride before use. Tetrahydrofuran and acetonitrile were used for synthesis (pro analysis grade) as received. The supporting electrolyte nBu$_4$NPF$_6$ (prepared from saturated solutions of KPF_6 and nBuN_4Br in water) was recrystallized from hot methanol and dried under vacuum at 80°C overnight. The phosphole ligand was synthesized according to a procedure in the literature (*21*). The acid Et_3NHBF_4 was synthesized according to a modified procedure in the literature (*39*), where the crude product was extracted with dichloromethane to remove residual NH_4BF_4. All commercially available chemicals were used as received.

Synthesis of 1

Fe_2(μ-bdt)$(CO)_6$ (1.0 g, 2.4 mmol), ligand (0.63 g, 1.7 mmol), and tetrahydrofuran (250 ml) were added to a 500-ml round-bottom flask. The solution was refluxed for 4 hours, and the crude product was purified on silica by eluting with pentane [elutes 0.40 g of Fe_2(μ-bdt)$(CO)_6$] and then 5% methanol in dichloromethane containing 1 drop of NH_4OH per 100 ml (elutes the product). Removal of solvent yielded 0.60 g (46%) of the product as a red powder. ^{1}H NMR (400 MHz, CD_2Cl_2) δ 8.50 (br s, 4*H*), 7.92 (ddd, *J* = 11.3, 8.0, 1.6 Hz, 2*H*), 7.66 (tdd, *J* = 8.7, 4.7, 2.2 Hz, 3*H*), 7.06 (br s, 4*H*), 7.01 (dd, *J* = 5.5, 3.2 Hz, 2*H*), 6.70 (dd, *J* = 5.4, 3.2 Hz, 2*H*), 2.66 (d, *J* = 17.6 Hz, 2*H*), 2.38 (d, *J* = 17.9 Hz, 2*H*), 1.61 (m, 4*H*). ^{31}P NMR (162 MHz, CD_2Cl_2) δ 75.1 (s). IR (CH_2Cl_2, cm^{-1}): ν(CO) 2053 (s), 1995 (s), 1983 (m), 1941 (w). Mass spectrometry [field desorption (FD^+)] for $C_{35}H_{25}Fe_2N_2O_5PS_2$: *m*/*z* 759.96413 (calculated), 759.96755 (observed) [Δ(*m*/*z*) = 4.50 ppm].

Synthesis of $\mathbf{1}^{Ph}$

A solution of Fe_2(μ-bdt)$(CO)_6$ (84.0 mg, 0.2 mmol) and ligand (73.3 mg, 0.2 mmol) in dichloromethane (20 ml) was treated with 4.0 ml of a 0.05 M solution of trimethylamine *N*-oxide dihydrate in acetonitrile. The solution was stirred at room temperature for 2 hours, and the crude product was purified on silica by eluting with pentane [elutes Fe_2(μ-bdt)$(CO)_6$] and then dichloromethane/pentane (2:5) (elutes the product). Removal of solvent yielded 71 mg (45%) of the product as a red powder. ^{1}H NMR (400 MHz, CD_2Cl_2) δ 7.95 (ddd, *J* = 11.0, 7.5, 2.1 Hz, 2*H*), 7.69 to 7.56 (m, 3*H*), 7.33 to 7.11 (m, 10*H*), 7.01 (dd, *J* = 5.5, 3.2 Hz, 2*H*), 6.68 (dd, *J* = 5.5, 3.2 Hz, 2*H*), 2.63 (d, *J* = 17.6 Hz, 2*H*), 2.35 (d, *J* = 18.3 Hz, 2*H*), 1.57 (4*H*, overlaps with water peak). ^{31}P NMR (162 MHz, CD_2Cl_2) δ 74.9 (s). IR (CH_2Cl_2, cm^{-1}): ν(CO) 2048 (s), 1992 (s), 1977 (m), 1939 (w). Mass spectrometry (FD^+) for $C_{37}H_{27}Fe_2O_5PS_2$: *m*/*z* 757.97363 (calculated), 757.98919 (observed) [Δ(*m*/*z*) = 20.5 ppm].

Synthesis of $Et_2\mathbf{1}\cdot(BF_4)_2$

A solution of **1** (7.6 mg, 10 μmol) in dichloromethane (5.0 ml) was treated with a solution of $Et_3O\cdot BF_4$ (0.50 ml of 0.040 M in dichloromethane, 20 μmol) and stirred at room temperature for 10 min. All of the solvent was evaporated, and the residue was dissolved in dichloromethane and filtered through a polytetrafluoroethylene filter (pore size, 0.45 μm). Removal of solvent yielded the product as a red solid in quantitative yield. ^{1}H NMR (400 MHz, CD_2Cl_2) δ 8.69 to 8.52 (m, 4*H*), 7.93 to 7.63 (m, 7*H*), 7.49 to 7.40 (m, 2*H*), 7.12 to 6.92 (m, 2*H*), 6.86 to 6.68 (m, 2*H*), 4.85 to 4.75 (m, 2*H*), 4.63 to 4.51 (m, 2*H*), 1.77 to 1.56 (m, 4*H*), 1.37 to 1.21 (m, 7*H*), 0.93 to 0.84 (m, 3*H*). ^{31}P NMR (162 MHz, CD_2Cl_2) δ 77.5 (s). IR (CH_2Cl_2, cm^{-1}): ν(CO) 2060 (s), 2002 (s), 1991 (m), 1945 (w), 1632 (w).

Electrochemistry in dichloromethane

Cyclic voltammetry was performed on 0.5 or 1 mM solutions of **1** in dichloromethane containing 0.1 M nBu$_4$NPF$_6$ as the supporting electrolyte. The voltammograms were recorded using a 663-VA stand with a PGSTAT302N potentiostat (Metrohm/Autolab), a static mercury drop electrode (drop size 2) as a working electrode, a glassy carbon rod as an auxiliary electrode, and a leakless $Ag^{0/+}$ reference electrode (eDAQ ET069). Single equivalents of Et_3NHBF_4 were added as a 25% m/v solution in dichloromethane. To convert the potential values of the $Ag^{0/+}$ reference into $Fc^{0/+}$, a correction factor was used, as determined by cyclic voltammetry of 1 mM ferrocene in dichloromethane using the same reference electrode. At the end of each experiment, ferrocene

was added to the solution to check for reference electrode drift. All cyclic voltammetric experiments in dichloromethane (except when measuring catalytic waves) were compensated to about 95% of solution resistance.

Electrochemistry in 1 M H_2SO_4 and in acidified 1 M Na_2SO_4

Cyclic voltammetry was performed on deoxygenated solutions, unless stated otherwise. Compound **1** was added as a 2 mM solution in methanol. The voltammograms were recorded using a 663-VA stand with a PGSTAT302N potentiostat (Metrohm/Autolab), a AuHg wire as a working electrode (vide infra), a platinum wire as an auxiliary electrode, and a Ag/AgCl (3 M KCl) reference electrode (Metrohm 6.0750.100). To convert the potential values of the $Ag^{0/+}$ reference into NHE, a correction factor of +0.21 V was used. The working electrode was a gold wire (0.5 mm in diameter, 99.99%; Sigma-Aldrich 310980) soldered to a copper wire (using a Sn/Pb eutectic solder), with the copper wire, solder joint, and part of the gold wire molten into a polyethylene housing. The gold wire was cut to leave 3 to 5 mm exposed. Before the experiments, the wire was thoroughly rinsed with ethanol, dried, submerged in (triply distilled) mercury for 5 min, wiped well with a dry tissue (repeated three times; a flat and shiny surface should be obtained), and placed diagonally in a glass cell approximately 5 mm from the reference electrode. All measurements were performed as automated sequences to maximize reproducibility. Six voltammograms were recorded in each sequence, with only scan rate varying (0.1, 0.3, 1.0, 3.0, 10, and 0.1 V s^{-1}). Before each scan, the solution was purged with N_2 for 10 s (while stirring) and then left undisturbed for 5 s.

DFT calculations

The gas-phase geometries of molecules **1**, $\mathbf{1}^{-}$, and $\mathbf{1}^{2-}$ were optimized with the Turbomole program package (*40*) at the ri-DFT (*41*)/BP86 (*42*, *43*) level. We used the def2-TZVP basis set (*44*, *45*) for all atoms. These calculations also yielded the frontier orbitals and spin density plots.

Time-resolved IR spectroscopy

Using a previously described experimental setup (*26*), we generated a visible pump and a mid-IR probe. Two commercial beta barium borate (BBO)-based optical parametric amplifiers (OPAs; Spectra-Physics OPA-800C) were pumped by a Ti:sapphire laser (Spectra-Physics Hurricane, 600 μJ) at a repetition rate of 1 kHz. IR probe pulses were generated by difference-frequency mixing signal and idler from one of the OPAs in a $AgGaS_2$ crystal. The visible pump pulses (630 nm; pulse energy, 3 μJ) were generated by doubling the signal of the other OPA. The delay positions were scanned by mechanically adjusting the beam path of the UV pump using a Newport ESP300 translation stage. The sample cell with CaF_2 windows spaced 500 μm apart was placed in the IR focus. From the full width at half-maximum of the pump probe cross-correlation function, a temporal resolution of 200 fs was obtained. A custom-built 30-pixel mercury cadmium telluride (MCT) detector coupled to an Oriel MS260i spectrograph was used to record the transient spectra by subtracting nonpumped absorption spectra from the pumped absorption spectra.

SUPPLEMENTARY MATERIALS

Supplementary material for this article is available at http://advances.sciencemag.org/cgi/content/full/2/1/e1501014/DC1

Materials and Methods

Fig. S1. Solution IR spectra of **1**, $\mathbf{1}^{Ph}$, and $Et_2\mathbf{1}\cdot(BF_4)_2$ in dichloromethane.
Fig. S2. ^1H NMR (400 MHz) of **1** in CD_2Cl_2.
Fig. S3. ^{31}P NMR (162 MHz) of **1** in CD_2Cl_2.
Fig. S4. $^1H^1H$ correlation spectroscopy (COSY; 300 MHz) of **1** in CD_2Cl_2.
Fig. S5. Nuclear Overhauser effect spectroscopy (NOESY; 300 MHz) of **1** in CD_2Cl_2.
Fig. S6. ^1H NMR (400 MHz) of $\mathbf{1}^{Ph}$ in CD_2Cl_2.
Fig. S7. ^{31}P NMR (162 MHz) of $\mathbf{1}^{Ph}$ in CD_2Cl_2.
Fig. S8. FD mass analysis of **1**.
Fig. S9. FD mass analysis of $\mathbf{1}^{Ph}$.
Fig. S10. X-ray diffraction structure of $\mathbf{1}^{Ph}$ with displacement ellipsoids at 50% probability.
Fig. S11. Bulk electrolysis of 10 μmol **1** on a carbon sponge electrode.
Fig. S12. Integrated data from fig. S11.
Fig. S13. Cyclic voltammograms of 0.5 mM **1**.
Fig. S14. Cyclic voltammograms of 0.5 mM **1**, starting from −1.6 V to the cathodic peak, then cycling over the reoxidation wave.
Fig. S15. Simulation of cyclic voltammograms (DigiElch) from fig. S13 (scan rate, 0.1 V s^{-1}).
Fig. S16. Simulation of cyclic voltammograms (DigiElch) from fig. S13 (scan rate, 1.0 V s^{-1}).
Fig. S17. UV-vis spectra of **1** and ZnTPP at a path length of 10 mm.
Fig. S18. UV-vis titration of a constant concentration of 80 μM ZnTPP with increasing equivalents **1**.
Fig. S19. Output of the fitting procedure.
Fig. S20. Fluorescence quenching titration of a constant concentration of ZnTPP with **1**.
Fig. S21. UV-vis spectrum of the sample used in the TR-IR experiment (path length, 500 μm).
Fig. S22. Rise and decay profiles plus global biexponential fitting from TR-IR at four wavelength maxima.
Fig. S23. Cyclic voltammograms of 0.5 mM **1** and 4.0 mM Et_3NHBF_4.
Fig. S24. Cyclic voltammograms of 0.5 mM **1** and 8.0 mM Et_3NHBF_4.
Fig. S25. Cyclic voltammograms of 0.5 mM **1** and 16 mM Et_3NHBF_4.
Fig. S26. Cyclic voltammograms of 0.5 mM **1** and 32 mM Et_3NHBF_4.
Fig. S27. ^1H NMR (400 MHz) of **1** in CD_2Cl_2 in the absence and presence of 4 eq of Et_3NHBF_4.
Fig. S28. Cathodic peak potential versus ln(scan rate).
Fig. S29. Cathodic peak potential versus ln([acid]^2).
Fig. S30. Simulation of cyclic voltammograms from fig. S23.
Fig. S31. Differential spectral evolution (pyridine region shown) going from **1** to **2**.
Fig. S32. Differential spectral evolution (pyridine region shown) going from **2** to **3** and then to $\mathbf{1}^{3-}$.
Fig. S33. Cyclic voltammogram of 1 mM **1** and 4.0 mM Et_3NHBF_4 and fits for the simulated model.
Fig. S34. Cyclic voltammograms of 1.0 mM $\mathbf{1}^{Ph}$.
Fig. S35. Cyclic voltammograms of 1.0 mM $\mathbf{1}^{Ph}$ in the presence of 8.0 mM Et_3NHBF_4.
Fig. S36. Cathodic peak potential versus ln(scan rate) and ln([acid]).
Fig. S37. Foot-of-the-wave analysis of the voltammograms in Fig. 8A.
Fig. S38. Synthesis and structure of $Et_2\mathbf{1}\cdot(BF_4)_2$.
Fig. S39. ^1H NMR (400 MHz) of $Et_2\mathbf{1}\cdot(BF_4)_2$ in CD_2Cl_2.
Fig. S40. ^{31}P NMR (162 MHz) of $Et_2\mathbf{1}\cdot(BF_4)_2$ in CD_2Cl_2.
Fig. S41. Cyclic voltammograms of 2 μM $Et_2\mathbf{1}\cdot(BF_4)_2$ in 0.1 M Na_2SO_4.
Fig. S42. Peak current versus scan rate for the adsorption waves in fig. S41.
Fig. S43. Cyclic voltammogram of 1 M H_2SO_4 (background currents).
Fig. S44. Cyclic voltammogram of 2 μM phosphole ligand in 1 M H_2SO_4.
Table S1. Comparison of the IR and NMR data of **1**, $\mathbf{1}^{Ph}$, and reference compounds.
Table S2. Fitted parameters (DigiElch) for the redox processes of **1** in the absence of acid.
Table S3. Calculated molar extinction coefficients and R^2 value of the fit.
Table S4. Titration setup (with equivalents **1** with respect to ZnTPP) measured and corrected intensity at 645 nm and free ZnTPP concentration.
Table S5. Fitted parameters for cyclic voltammogram as shown in figs. S23 to S26.
Table S6. Comparison of reduced and protonated 4,4′-bipyridine species with species formed during spectroelectrochemical reduction in the presence of acid.
Table S7. Model parameters for cyclic voltammogram as shown in fig. S33.
Table S8. TON during one cyclic voltammogram scan at various scan rates.
References (*46*–*48*)

REFERENCES AND NOTES

1. R. Sathre, C. D. Scown, W. R. Morrow III, J. C. Stevens, I. D. Sharp, J. W. Ager III, K. Walczak, F. A. Houle, J. B. Greenblatt, Life-cycle net energy assessment of large-scale hydrogen production via photoelectrochemical water splitting. *Energy Environ. Sci.* **7**, 3264–3278 (2014).
2. M. Carmo, D. L. Fritz, J. Mergel, D. Stolten, A comprehensive review on PEM water electrolysis. *Int. J. Hydrogen Energy* **38**, 4901–4934 (2013).
3. F. A. Armstrong, Hydrogenases: Active site puzzles and progress. *Curr. Opin. Chem. Biol.* **8**, 133–140 (2004).
4. N. Plumeré, O. Rüdiger, A. A. Oughli, R. Williams, J. Vivekananthan, S. Pöller, W. Schuhmann, W. Lubitz, A redox hydrogel protects hydrogenase from high-potential deactivation and oxygen damage. *Nat. Chem.* **6**, 822–827 (2014).

5. T. R. Simmons, G. Berggren, M. Bacchi, M. Fontecave, V. Artero, Mimicking hydrogenases: From biomimetics to artificial enzymes. *Coord. Chem. Rev.* **270–271**, 127–150 (2014).
6. C. Tard, C. J. Pickett, Structural and functional analogues of the active sites of the [Fe]-, [NiFe]-, and [FeFe]-hydrogenases. *Chem. Rev.* **109**, 2245–2274 (2009).
7. J. R. McKone, S. C. Marinescu, B. S. Brunschwig, J. R. Winkler, H. B. Gray, Earth-abundant hydrogen evolution electrocatalysts. *Chem. Sci.* **5**, 865–878 (2014).
8. P. Du, R. Eisenberg, Catalysts made of earth-abundant elements (Co, Ni, Fe) for water splitting: Recent progress and future challenges. *Energy Environ. Sci.* **5**, 6012–6021 (2012).
9. M. Wang, L. Chen, L. Sun, Recent progress in electrochemical hydrogen production with earth-abundant metal complexes as catalysts. *Energy Environ. Sci.* **5**, 6763–6778 (2012).
10. V. S. Thoi, Y. Sun, J. R. Long, C. J. Chang, Complexes of earth-abundant metals for catalytic electrochemical hydrogen generation under aqueous conditions. *Chem. Soc. Rev.* **42**, 2388–2400 (2013).
11. G. Berggren, A. Adamska, C. Lambertz, T. R. Simmons, J. Esselborn, M. Atta, S. Gambarelli, J.-M. Mouesca, E. Reijerse, W. Lubitz, T. Happe, V. Artero, M. Fontecave, Biomimetic assembly and activation of [FeFe]-hydrogenases. *Nature* **499**, 66–69 (2013).
12. J. Esselborn, C. Lambertz, A. Adamska-Venkatesh, T. Simmons, G. Berggren, J. Noth, J. Siebel, A. Hemschemeier, V. Artero, E. Reijerse, M. Fontecave, W. Lubitz, T. Happe, Spontaneous activation of [FeFe]-hydrogenases by an inorganic [2Fe] active site mimic. *Nat. Chem. Biol.* **9**, 607–609 (2013).
13. M. L. Helm, M. P. Stewart, R. M. Bullock, M. R. DuBois, D. L. DuBois, A synthetic nickel electrocatalyst with a turnover frequency above 100,000 s^{-1} for H_2 production. *Science* **333**, 863–866 (2011).
14. R. M. Bullock, A. M. Appel, M. L. Helm, Production of hydrogen by electrocatalysis: Making the H–H bond by combining protons and hydrides. *Chem. Commun.* **50**, 3125–3143 (2014).
15. J. Hou, M. Fang, A. J. P. Cardenas, W. J. Shaw, M. L. Helm, R. M. Bullock, J. A. S. Roberts, M. O'Hagan, Electrocatalytic H_2 production with a turnover frequency $>10^7$ s^{-1}: The medium provides an increase in rate but not overpotential. *Energy Environ. Sci.* **7**, 4013–4017 (2014).
16. A. Adamska-Venkatesh, D. Krawietz, J. Siebel, K. Weber, T. Happe, E. Reijerse, W. Lubitz, New redox states observed in [FeFe] hydrogenases reveal redox coupling within the H-cluster. *J. Am. Chem. Soc.* **136**, 11339–11346 (2014).
17. C. Tard, X. Liu, S. K. Ibrahim, M. Bruschi, L. De Gioia, S. C. Davies, X. Yang, L.-S. Wang, G. Sawers, C. J. Pickett, Synthesis of the H-cluster framework of iron-only hydrogenase. *Nature* **433**, 610–613 (2005).
18. J. M. Camara, T. B. Rauchfuss, Combining acid–base, redox and substrate binding functionalities to give a complete model for the [FeFe]-hydrogenase. *Nat. Chem.* **4**, 26–30 (2012).
19. J. C. Lansing, J. M. Camara, D. E. Gray, T. B. Rauchfuss, Hydrogen production catalyzed by bidirectional, biomimetic models of the [FeFe]-hydrogenase active site. *Organometallics* **33**, 5897–5906 (2014).
20. M. Stolar, T. Baumgartner, Phosphorus-containing materials for organic electronics. *Chem. Asian J.* **9**, 1212–1225 (2014).
21. C. Lescop, L. Toupet, R. Réau, Syntheses and coordination chemistry of bis(4-pyridyl)- and mixed (4-pyridyl) (2-pyridyl)-phospholes. *Heteroatom Chem.* **22**, 339–347 (2011).
22. A. M. Kluwer, R. Kapre, F. Hartl, M. Lutz, A. L. Spek, A. M. Brouwer, P. W. N. M. van Leeuwen, J. N. H. Reek, Self-assembled biomimetic [2Fe2S]-hydrogenase–based photocatalyst for molecular hydrogen evolution. *Proc. Natl. Acad. Sci. U.S.A.* **106**, 10460–10465 (2009).
23. V. D. Parker, Electrode mechanism analysis by linear sweep voltammetry. III. Reaction orders, the origin of the response. *Acta Chem. Scand.* **35**, 259–262 (1981).
24. P. Hapiot, L. D. Kispert, V. V. Konovalov , J.-M. Savéant, Single two-electron transfers vs successive one-electron transfers in polyconjugated systems illustrated by the electrochemical oxidation and reduction of carotenoids. *J. Am. Chem. Soc.* **123**, 6669–6677 (2001).
25. P. Adkine, T. Cantat, E. Deschamps, L. Ricard, N. Mézailles, P. Le Floch, M. Geoffroy, EPR and DFT studies of the one-electron reduction product of phospholium cations. *Phys. Chem. Chem. Phys.* **8**, 862–868 (2006).
26. P. Li, S. Amirjalayer, F. Hartl, M. Lutz, B. de Bruin, R. Becker, S. Woutersen, J. N. H. Reek, Direct probing of photoinduced electron transfer in a self-assembled biomimetic [2Fe2S]-hydrogenase complex using ultrafast vibrational spectroscopy. *Inorg. Chem.* **53**, 5373–5383 (2014).
27. M. Mirmohades, S. Pullen, M. Stein, S. Maji, S. Ott, L. Hammarström, R. Lomoth, Direct observation of key catalytic intermediates in a photoinduced proton reduction cycle with a diiron carbonyl complex. *J. Am. Chem. Soc.* **136**, 17366–17369 (2014).
28. G. A. N. Felton, A. K. Vannucci, J. Chen, L. T. Lockett, N. Okumura, B. J. Petro, U. I. Zakai, D. H. Evans, R. S. Glass, D. L. Lichtenberger, Hydrogen generation from weak acids: Electrochemical and computational studies of a diiron hydrogenase mimic. *J. Am. Chem. Soc.* **129**, 12521–12530 (2007).
29. A. S. Pereira, P. Tavares, I. Moura, J. J. G. Moura, B. H. Huynh, Mössbauer characterization of the iron–sulfur clusters in *Desulfovibrio vulgaris* hydrogenase. *J. Am. Chem. Soc.* **123**, 2771–2782 (2001).
30. S. Ezzaher, A. Gogoll, C. Bruhn, S. Ott, Directing protonation in [FeFe] hydrogenase active site models by modifications in their second coordination sphere. *Chem. Commun.* **46**, 5775–5777 (2010).
31. N. Wang, M. Wang, L. Chen, L. Sun, Reactions of [FeFe]-hydrogenase models involving the formation of hydrides related to proton reduction and hydrogen oxidation. *Dalton Trans.* **42**, 12059–12071 (2013).
32. F. I. Adam, G. Hogarth, S. E. Kabir, I. Richards, Models of the iron-only hydrogenase: Synthesis and protonation of bridge and chelate complexes $[Fe_2(CO)_4\{Ph_2P(CH_2)_nPPh_2\}(\mu\text{-pdt})]$ (n = 2–4)—Evidence for a terminal hydride intermediate. *C R Chim.* **11**, 890–905 (2008).
33. G. Buntinx, P. Valat, V. Wintgens, O. Poizat, Photoreduction of 4,4′-bipyridine by triethylamine and by 1,4-diazabicyclo[2.2.2]octane in acetonitrile as studied by nanosecond absorption and Raman spectroscopies. *J. Phys. Chem.* **95**, 9347–9352 (1991).
34. C. Costentin, S. Drouet, M. Robert, J.-M. Savéant, Turnover numbers, turnover frequencies, and overpotential in molecular catalysis of electrochemical reactions. Cyclic voltammetry and preparative-scale electrolysis. *J. Am. Chem. Soc.* **134**, 11235–11242 (2012).
35. J. Moiroux, S. Deycard, T. Malinski, Electrochemical reduction of NAD^+ and pyridinium cations adsorbed at the mercury/water interface: Electrochemical behavior of adsorbed pyridinyl radicals. *J. Electroanal. Chem. Interfacial Electrochem.* **194**, 99–108 (1985).
36. C. Costentin, G. Passard, J.-M. Savéant, Benchmarking of homogeneous electrocatalysts: Overpotential, turnover frequency, limiting turnover number. *J. Am. Chem. Soc.* **137**, 5461–5467 (2015).
37. J.-M. Savéant, *Elements of Molecular and Biomolecular Electrochemistry: An Electrochemical Approach to Electron Transfer Chemistry* (Wiley, Hoboken, NJ, 2006).
38. V. Artero, J. M. Savéant, Toward the rational benchmarking of homogeneous H_2-evolving catalysts. *Energy Environ. Sci.* **7**, 3808–3814 (2014).
39. S. Saba, R. Hernandez, C. Chin Choy, K. Carta, Y. Bennett, S. Bondi, S. Kolaj, C. Bennett, A simple and efficient one-step protocol for the preparation of alkyl-substituted ammonium tetrafluoroborate and hexafluorophosphate salts. *J. Fluorine Chem.* **153**, 168–171 (2013).
40. R. Ahlrichs, TURBOMOLE V6.5 2013 (a development of University of Karlsruhe and Forschungszentrum Karlsruhe GmbH, 1989–2007; TURBOMOLE GmbH, since 2007); available at www.turbomole.com.
41. M. Sierka, A. Hogekamp, R. Ahlrichs, Fast evaluation of the Coulomb potential for electron densities using multipole accelerated resolution of identity approximation. *J. Chem. Phys.* **118**, 9136–9148 (2003).
42. A. D. Becke, Density-functional exchange-energy approximation with correct asymptotic behavior. *Phys. Rev. A* **38**, 3098–3100 (1988).
43. J. P. Perdew, Density-functional approximation for the correlation energy of the inhomogeneous electron gas. *Phys. Rev. B Condens. Matter* **33**, 8822–8824 (1986).
44. F. Weigend, R. Ahlrichs, Balanced basis sets of split valence, triple zeta valence and quadruple zeta valence quality for H to Rn: Design and assessment of accuracy. *Phys. Chem. Chem. Phys.* **7**, 3297–3305 (2005).
45. F. Weigend, M. Häser, H. Patzelt, R. Ahlrichs, RI-MP2: Optimized auxiliary basis sets and demonstration of efficiency. *Chem. Phys. Lett.* **294**, 143–152 (1998).
46. M. Krejčík, M. Daněk, F. Hartl, Simple construction of an infrared optically transparent thin-layer electrochemical cell: Applications to the redox reactions of ferrocene, $Mn_2(CO)_{10}$ and $Mn(CO)_3$(3,5-di-*t*-butyl-catecholate)$^-$. *J. Electroanal. Chem. Interfacial Electrochem.* **317**, 179–187 (1991).
47. J. A. Cabeza, M. A. Martínez-García, V. Riera, Binuclear iron(I), ruthenium(I), and osmium(I) hexacarbonyl complexes containing a bridging benzene-1,2-dithiolate ligand. Synthesis, X-ray structures, protonation reactions, and EHMO calculations. *Organometallics* **17**, 1471–1477 (1998).
48. Y.-C. Liu, T.-H. Yen, Y.-J. Tseng, C.-H. Hu, G.-H. Lee, M.-H. Chiang, Electron delocalization from the fullerene attachment to the diiron core within the active-site mimics of [FeFe] hydrogenase. *Inorg. Chem.* **51**, 5997–5999 (2012).
49. F. Gloaguen, D. Morvan, J.-F. Capon, P. Schollhammer, J. Talarmin, Electrochemical proton reduction at mild potentials by monosubstituted diiron organometallic complexes bearing a benzenedithiolate bridge. *J. Electroanal. Chem.* **603**, 15–20 (2007).

Acknowledgments: We thank J. I. van der Vlugt for determining the x-ray diffraction structure of compound $\mathbf{1^{Ph}}$, E. Zuidinga for mass analysis, T. Kumpulainen for help with fluorescence spectroscopy, S. Leenders for help with NOESY and COSY measurements, C. Rebreyend for help with EPR spectroscopy, and R. Zaffaroni and R. Detz for fruitful discussions. **Funding:** This work was supported by the BioSolar Cells program (R.B.) and the National Research School Combination Catalysis (P.L.). **Author contributions:** R.B. designed the experiments; performed synthesis, characterization, (spectro)electrochemistry, and data analysis; and wrote the paper. P.L. performed DFT calculations. S.A. and S.W. performed TR-IR. J.N.H.R. designed the experiments, performed data analysis, and wrote the paper. **Competing interests:** The authors declare that they have no competing interests. **Data and materials availability:** All data needed to evaluate the conclusions in the paper are present in the paper and/or the Supplementary Materials. Additional data related to this paper may be requested from the authors.

Submitted 30 July 2015
Accepted 18 November 2015
Published 22 January 2016
10.1126/sciadv.1501014

Citation: R. Becker, S. Amirjalayer, P. Li, S. Woutersen, J. N. H. Reek, An iron-iron hydrogenase mimic with appended electron reservoir for efficient proton reduction in aqueous media. *Sci. Adv.* **2**, e1501014 (2016).